

Moderate-terahertz-induced plateau expansion of high-order harmonic generation to soft X-ray region

Doan-An Trieu,^{1, 2, *} Duong D. Hoang-Trong,^{3, 4} Cam-Tu Le,^{5, 6} Sang Ha,⁷ Ngoc-Hung Phan,⁷ F. V. Potemkin,⁸ Van-Hoang Le,⁷ and Ngoc-Loan Phan^{7, †}

¹ Institute of Fundamental and Applied Sciences,

Duy Tan University, Ho Chi Minh City 700000, Vietnam

² Faculty of Natural Sciences, Duy Tan University, Da Nang City 550000, Vietnam

³ Simulation in Materials Science Research Group, Science and Technology Advanced Institute,

Van Lang University, Ho Chi Minh City, Vietnam

⁴ Faculty of Applied Technology, School of Technology,

Van Lang University, Ho Chi Minh City, Vietnam

⁵ Atomic Molecular and Optical Physics Research Group,

Ton Duc Thang University, Ho Chi Minh City 72915, Vietnam

⁶ Faculty of Applied Sciences, Ton Duc Thang University, Ho Chi Minh City 72915, Vietnam

⁷ Computational Physics Key Laboratory K002, Department of Physics,

Ho Chi Minh City University of Education, Ho Chi Minh City 72711, Vietnam

⁸ Faculty of Physics, M. V. Lomonosov Moscow State University,

Leninskie Gory 1/2, Moscow 119991, Russian Federation

(Dated: January 26, 2026)

Extending the high-harmonic cutoff with experimentally accessible fields is essential for advancing tabletop coherent extreme ultraviolet (EUV) and soft X-ray sources. Although terahertz (THz) assistance offers a promising route, cutoff extension at weak, laboratory-accessible THz strengths remain poorly understood. In this report, we comprehensively investigate THz-assisted high-order harmonic generation (HHG) using time-dependent Schrödinger equation simulations supported by classical trajectory analysis and Bohmian-based quantum dynamics. By mapping the plateau evolution versus THz strength, we show that even weak THz fields can extend the cutoff, producing a pronounced “fish-fin” structure whose prominent rays saturate near $I_p + 8U_p$. We trace this extension to long electron excursions spanning several optical cycles before recombination, and provide a fully consistent explanation using both classical analysis and Bohmian trajectories flow. Our findings reveal that this cutoff-extension mechanism is remarkably robust, persisting across different atomic species and remaining insensitive to variations in the driving parameters. These results demonstrate that cutoff control is achievable with laboratory-scale THz fields, offering practical guidelines for engineering coherent high-energy HHG, and providing a robust pathway for tracking ultrafast electron motion in real time.

I. INTRODUCTION

High-order harmonic generation (HHG), arising from the intense laser-matter interaction, has increasingly emerged as a powerful tabletop source of extreme ultraviolet (EUV) to X-ray radiation, underpinning major advances in strong-field physics and attosecond science [1–8]. Although HHG from condensed media has recently been explored, gas-phase HHG remains the most effective route for generating high-energy coherent radiation because gases support higher cutoff energies than denser media [4, 9, 10]. The conventional gas-phase cutoff, given by $I_p + 3.17U_p$ (with I_p the ionization potential and U_p the ponderomotive energy), is intuitively explained by the three-step model [11, 12].

Over the past two decades, extensive efforts have been devoted to broadening the HHG spectrum. Among various strategies, field engineering to tailor electron paths has proven particularly effective [13–24]. A particularly simple and effective approach is to superimpose

a static electric field on the fundamental infrared (IR) laser pulse, which can theoretically extend the cutoff up to $I_p + 9.1U_p$ [16–19, 25–31]. However, reaching this extension requires a static field about 39% of the fundamental field (of order 100 MV/cm) [16–19, 25–28], which remains experimentally challenging [28, 32, 33].

Recent advances in terahertz (THz) technology have enabled the use of THz fields as a dynamic substitute for static fields in HHG [28, 34, 35], opening new opportunities for retrieving both target structural dynamics and THz-field temporal profiles [28, 34, 36–40]. The THz fields used in such THz-assisted HHG experiments are typically weak, only a few percent of the IR field strength, and can be readily generated by standard tabletop techniques [28, 34, 35]. However, extending the harmonic cutoff by THz assistance generally requires strong-field THz amplitudes (about of 100 MV/cm) [16, 17, 28], which only a few specialized laboratories can generate due to poor conversion, strict damage limits, and propagation near air breakdown [32, 33]. Therefore, developing schemes that can extend the harmonic plateau using readily accessible low-field THz remains an important challenge.

In addition, weak static electric fields have been

* trieudoan@duytan.edu.vn

† loanptn@hcmue.edu.vn (Corresponding author)

shown to induce multiple HHG plateaus, indicating an extended cutoff [16, 25, 26]. This suggests that experimentally accessible weak THz fields may also enable cutoff extension. However, no clear rule has yet been established for how weak THz fields govern this extension, nor whether the resulting plateaus occur only at particular THz strengths or persist over a broader range. This gap underscores the need for a systematic investigation of cutoff behavior as a function of THz field strength.

In this work, we systematically map the plateau evolution in THz-assisted HHG as a function of THz-field strength to identify the regimes accessible with laboratory-scale sources. To this end, we first solve the time-dependent Schrödinger equation (TDSE) of atoms exposed to the combined IR-THz fields. To uncover the underlying physics, we complement these calculations with classical trajectory analysis and Bohmian-based quantum simulations. Atomic systems (hydrogen, helium, argon, neon) are used as reference targets.

This paper is organized as follows. Section II summarizes the computational methods, including TDSE simulations and the visualization of electron dynamics via classical and Bohmian-trajectory analyses. Section III presents comprehensive HHG spectra from atomic systems under varying THz strengths. We discuss the emergence of the “fish-fin” structure, and then establish the rule governing THz-induced cutoff extension through long-traveling electron trajectories. Finally, Sec. IV outlines the main findings and perspectives.

II. THEORETICAL FRAMEWORK FOR HHG CALCULATION AND ELECTRON-TRAJECTORY ANALYSIS

In this section, we first outline the method for simulating THz-assisted HHG and then describe the methods for analyzing electron trajectories.

A. Method for calculating THz-assisted HHG

We directly solve the TDSE of an atom exposed to a combined IR driving laser pulse and a THz field, which in the atomic units ($\hbar = m_e = e = 1$) is given by

$$i \frac{\partial}{\partial t} \psi(\mathbf{r}, t) = \left[-\frac{1}{2} \nabla^2 + V_c(\mathbf{r}) + \mathbf{r} \cdot \mathbf{E}(t) \right] \psi(\mathbf{r}, t), \quad (1)$$

where $\psi(\mathbf{r}, t)$ is the time-dependent wavefunction of the active electron, and $V_c(\mathbf{r})$ represents the atomic potential [41], whose further details are provided in Appendix A. Besides, $\mathbf{E}(t)$ is the combined electric field of the IR driving laser pulse and THz field whose polarizations are along the x axis. The combined field’s amplitude has the form

$$E(t) = E_0 f(t) \cos(\omega_0 t) + E_T \cos(\omega_T t) \quad (2)$$

which is defined within the time interval $[-\tau/2, \tau/2]$ where τ denotes the total duration of the IR pulse.

Here, E_0 and ω_0 are respectively the peak amplitude and carrier frequency of the IR pulse, while E_T and ω_T correspond to those of the THz field.

We directly solve the TDSE [Eq. (1)] (referred to as the TDSE method), in which the time-dependent wavefunction is evolved from the initial state using the split-operator algorithm [42–45]. The initial wavefunction is obtained numerically by the imaginary-time propagation method [46]. All numerical parameters are carefully checked to ensure convergence.

Once the time-dependent wavefunction is obtained, we calculate the laser-induced acceleration dipole using Ehrenfest’s theorem. The HHG intensity is then obtained as the squared modulus of the Fourier transform of the acceleration dipole. To analyze the temporal emission of HHG, we compute the harmonic time-frequency profile via the Gabor transform [47]. Details of the TDSE method are provided in Appendix B.

B. Methods for visualizing electron trajectories

To uncover the physics governing THz assisted HHG, we directly analyze electron motion in the combined fields. This subsection summarizes the classical and quantum trajectory methods employed.

1. Classical approach

According to the classical three-step model [11, 48], the electron’s motion after ionization can be treated classically. Along the polarization direction, its equation of motion reads

$$\ddot{x}(t) = -E(t), \quad (3)$$

with initial conditions $x(t_i) = \dot{x}(t_i) = 0$, where t_i is the ionization time.

By solving Eq. (3) for different ionization times, a swarm of classical trajectories is obtained. Most electrons are pulled away from the parent ion and are referred to as photoelectrons, while a few return to the parent ion, satisfying the returning condition $x(t_r) = 0$, where t_r is the return time. These “returning electrons” can recombine with the parent ion, emitting harmonics with energy $\Omega = I_p + K$, where K is the electron’s accumulated kinetic energy, given by $K = \frac{\dot{x}^2(t_r)}{2}$.

2. Quantum-based approach

We apply the pilot-wave theory of Bohmian mechanics [49–53] to describe the dynamics of the liberated electron, which is guided by the wave function $\psi(\mathbf{r}, t)$. Its guiding equation takes the form

$$\frac{d\mathbf{r}(t)}{dt} = \text{Im} \left[\frac{\nabla \psi(\mathbf{r}, t)}{\psi(\mathbf{r}, t)} \right]. \quad (4)$$

The solution for each initial position $\mathbf{r}(t=0)$ defines a “quantum” trajectory as it is guided by the wave function obtained from solving the TDSE (1). Such trajectories are referred to as Bohmian trajectories.

To reproduce the statistical predictions that match standard quantum mechanics, each trajectory is assigned a weight proportional to the initial probability [54] as $w_j = \int_{S_j} |\psi(\mathbf{r}, t=0)|^2 d\mathbf{r}$, where S_j denotes a small vicinity of 0.02 a.u. around initial electron position. The detailed calculation procedure is presented in our previous works [52, 53].

III. RESULTS AND DISCUSSIONS

In this section, we first present comprehensive results of HHG spectra from the hydrogen atom under gradually varying THz fields. The physical mechanisms are then elucidated through visualizations of electron trajectories obtained from both classical and quantum analyses.

A. Comprehensive view of THz-induced plateau expansion in HHG from atom

1. THz-assisted HHG: “fish-fin” structure

We investigate the HHG spectra from a hydrogen atom while gradually tuning the THz field strength, as shown in Fig. 1(a). For convenience, the left axis indicates the kinetic energy of the returning electron K , corresponding to harmonic photon energy $I_p + K$. The THz strength is quantified by $\alpha = E_T/E_0$, where E_T and E_0 are the amplitudes of the THz and driving laser fields, respectively. The 12-cycle driving laser pulse with flat-top envelope (four cycles ramp on and off), an intensity of 10^{14} W/cm², and a wavelength of 1200 nm is used. The THz frequency ω_T is fixed at 1.3 THz, corresponding to the wavelength of 231 μ m. These field parameters are selected as representative values to aid visualization.

The overall behavior of the HHG spectra [Fig. 1(a)] shows typical plateau structures with a sharp cutoff for all α values. However, the energy of *overall cutoff* does not vary smoothly with α , but instead forms a distinct “fish-fin” pattern with prominent rays. Particularly, as the THz field strength increases, the overall cutoff gradually extends from $I_p + 3.17U_p$ to $I_p + 8U_p$, with $U_p = E_0^2/4\omega_0^2$, reaching the EUV and soft-X-ray regions at $\alpha = 4\%$ ($E_T \approx 12$ MV/cm). The cutoff then fluctuates within a broad range of α within 4% – 40%. At $\alpha = 40\%$ ($E_T \approx 100$ MV/cm), the cutoff reaches a maximum of $I_p + 9.1U_p$, consistent with previous reports [16, 17, 25, 26, 28]. Beyond this point, it rapidly decreases as α further increases. This “fish-fin” behavior indicates that EUV and soft-X-ray coherent harmonics can be efficiently generated even under moderate THz

fields readily available in standard tabletop laboratories [28, 32–35].

In addition to the cutoff extension, Fig. 1(a) also reveals a clear *multiplateau structure* in HHG appearing when α exceed about 3%. Beyond the primary plateau (white solid curve), the number and shape of higher plateaus follow the “rays” of the “fish-fin” pattern. Although similar multiplateau structures were reported previously [25, 26], here we indicate that both the number and morphology of the plateaus vary noticeably with α , as depicted for α of 5% and 10% in Figs. 1[(a), (b2), (b3)]. For $\alpha > 10\%$, the number of plateaus decreases [Figs. 1(a),(b3), (b4)]. Apart from the structural changes, their cutoff behavior is also remarkable: Fig. 1(a) shows that the cutoff of the first plateau (red dashed curve) decreases, whereas the overall cutoff (white solid curve) continues to increase with noticeable fluctuations. As shown in Figs. 1[(b1)-(b4)], the first plateau’s cutoffs are respectively at the harmonic order 55, 51, 43, 21 for $\alpha = 0$, 5%, 10%, and 40%, while the corresponding overall cutoffs reach HHG order of 55, 107, 106, and 137.

Furthermore, we verify the appearance of the “fish-fin” structure and the associated plateau extension in other atomic targets driven by combined intense IR and THz fields. Numerical results for rare gas atoms such as He, Ne, and Ar (not shown) all exhibit clear “fish-fin” patterns similar to hydrogen, demonstrating that the THz induced extension is robust across different atomic species. We further varied the IR laser’s intensity and wavelength, and consistently recovered the same “fish-fin” structure, showing that the effect is robust against changes in the IR field. However, the IR intensity must be sufficiently strong to ionize the electron [55], yet still remain below the saturation intensity to avoid depletion, in which most electrons are driven too far from the core to return and recombine [56, 57]. These observations confirm that the “fish-fin” structure and the resulting cutoff extension is universal and experimentally accessible across a broad range of atomic systems.

Our observation of the “fish-fin” structure demonstrates that coherent EUV and soft X-ray harmonics can be generated using moderate THz fields of only ten to several tens of MV/cm, rather than the extremely strong fields on the order of 100 MV/cm suggested previously [16, 17, 25, 26, 28]. Importantly, THz fields in this amplitude range are accessible with tabletop laser-driven sources, such as optical rectification in organic nonlinear crystals and air-plasma-based schemes [28, 32–35]. In contrast, the generation of quasi-stationary THz fields approaching 100 MV/cm remains technologically challenging and typically requires either large-scale accelerator-based facilities, such as coherent transition radiation or free-electron-laser-based THz sources [58, 59], or sophisticated multi-crystal schemes relying on wide-aperture organic crystals combined with precise coherent field interference. Even reaching field strengths on the order of 50 MV/cm is highly nontrivial and has so far been demonstrated

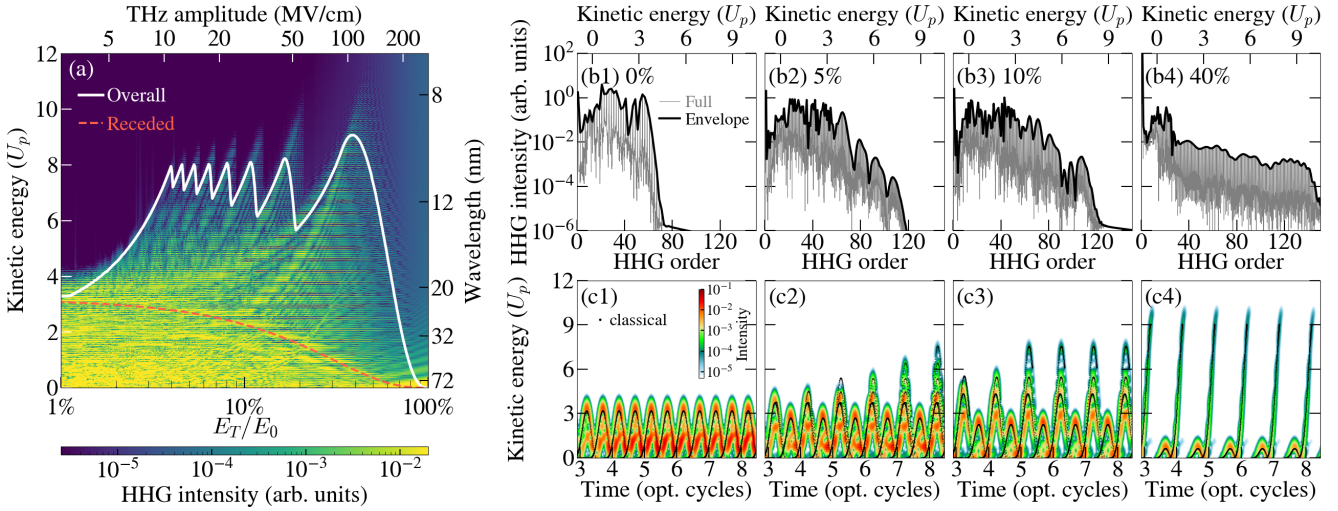


FIG. 1. (a) Comprehensive HHG spectra from the hydrogen atom in the combined IR-THz fields with varying THz strength, where the color encodes the HHG intensity. Panels [(b1)-(b4)] show detailed spectra, and Panels [(c1)-(c4)] display corresponding time-frequency profiles for specific THz fields, where $\alpha = E_T/E_0$ denotes the THz-to-IR amplitude ratio. In Panels [(b1)-(b4)], the gray curves represent the HHG spectra, whose envelope is demonstrated by the solid black curves. In Panels [(c1)-(c4)], the classical returning-electron kinetic-energy are shown by dotted curves. The comprehensive HHG spectra exhibits a “fish-fin” structure of the overall cutoff (white solid curve), where EUV harmonics can be generated under moderate THz fields. For α within 4%–40%, multiplateau structure emerges due to the imbalance between adjacent attosecond bursts, where one burst group forms the first plateau [red dashed curve in panel (a)] and the other contributes to its extension.

only in a handful of specialized laboratories worldwide. For example, achieving such field strengths requires a faceted assembly of four organic crystals pumped at 1.2–1.5 μm with pulse energies of ~ 30 mJ and fluences approaching 10 mJ/cm² [60], which can be realized using Cr:Forsterite-based laser systems [61]. Therefore, the observation of the “fish-fin” structure demonstrates that coherent soft X-ray harmonics can be accessed using experimentally realistic table-top THz field strengths, substantially relaxing the requirement for ultra-high THz fields previously considered necessary.

2. Time-frequency analysis: THz-dependent cutoff energies of emission bursts

To gain a deeper understanding of the “fish-fin” feature of spectral HHG, we further calculate the harmonic time-frequency (TF) profiles under varying THz fields, as shown in Figs. 1[(c1)-(c4)]. These profiles reveal that the harmonic emission occurs as a sequence of attosecond bursts separated by half an optical cycle. However, the behavior of these bursts varies significantly with the THz field. In the absence of the THz field, these bursts are identical owing to the inversion symmetry of the atomic target combined with a half-cycle time translation of the field [Fig. 1(c1)]. In contrast, the THz field breaks this symmetry, leading to an alternation between adjacent bursts (Figs. 1[(c2)-(c4)]). In these cases, the bursts can be categorized into two groups: the first corresponds to those emitted around $(3.2 + k)T_0$, and the second one to those emitted around $(3.7 + k)T_0$, where

$T_0 = 2\pi/\omega_0$ is an optical cycle and $k = 0 \div 8$.

Figures 1[(c1)-(c4)] show that, for each value of α , the bursts in the second group are identical, and their maximum photon energies are lower than those of the first group. Consequently, these bursts contribute to the formation of the first plateau, with the cutoff corresponding to their maximum energy. Moreover, as the THz field strength increases, their cutoff energies decrease rapidly, accounting for the recession of the first plateau cutoff in the spectral HHG, as marked by the red dashed curve in Fig. 1(a).

Meanwhile, the attosecond bursts of the first group exhibit diverse behaviors with varying THz fields. With small THz amplitude, e.g., $\alpha = 5\%$ in Fig. 1(c2), the cutoff of burst in the first group increases stepwise with time, leading to the formation of a multi-plateau structure. For a stronger field, such as $\alpha = 10\%$ in Fig. 1(c3), the cutoffs of the bursts emitted in the latter half of the laser pulse become identical, thereby reducing the number of plateaus. At higher field of $\alpha = 40\%$ [Fig. 1(c4)], the bursts regain uniformity, giving rise to the second plateau [16, 17, 25, 26, 28, 31]. This broadband second plateau, with nearly in-phase harmonics, is advantageous for generating attosecond pulse trains of extremely short duration [16, 17, 28].

In summary, the THz field alters the cutoff energies of attosecond bursts, which directly governs the formation, suppression, and disappearance of multiple plateaus in the HHG spectra. This underscores that the spectral features of HHG arise from the attosecond burst emission, which is governed by the temporal dynamics of electrons under the combined IR and THz fields, moti-

vating a detailed analysis of their trajectories.

B. Electron-trajectory analysis: Insights from classical and quantum frameworks

Although the multiplateau structure has been qualitatively explained for specific THz field strengths by classical electron trajectories [16, 17, 25, 26, 28, 31, 38–40], the physical origin of the “fish-fin” feature, characterized by its prominent ray-like patterns in the HHG spectra, remains unclear. In this section, we perform a detailed analysis of electron trajectories, employing both classical and quantum approaches, to elucidate the underlying mechanism.

1. Long-traveling trajectories and kinetic-energy saturation: classical and analytical analysis

First, we simulate the classical motion of an electron in the combined IR and THz fields following the procedure described in Sec. II B, and then perform an analytical analysis to interpret its trajectory dynamics. For simplicity, the IR pulse envelope is treated as a continuous wave [$f(t) = 1$].

Classical simulation

In Fig. 2, we show the accumulated kinetic energy of returning electrons at recombination (first row) and their corresponding trajectories (second and third rows) for α of 0%, 5%, 10% and 40%. Owing to the field periodicity, only results for electrons released within the first optical cycle are displayed in the first two rows. In the third row, the trajectories are periodically replicated until the end of the IR pulse.

Figures 2[(a1), (b1), (c1)] show that in the THz-free case ($\alpha = 0$), the kinetic energy across the two half-cycles is identical due to symmetric electron propagation on both sides of the hydrogen atom. Moreover, as indicated by gray curves, the electron exceeding a distance of approximately $2r_q$ (with $r_q = E_0/\omega_0^2$ being quiver amplitude) cannot return to recombine to the parent ion. Consequently, the maximum kinetic energy is limited by $3.17U_p$ [11, 12].

We now consider the case of a weak THz field with $\alpha = 5\%$. Figure 2(b2) clearly indicates that the additional THz field breaks the electron trajectory propagation between the two sides of the atom. Specifically, in the $x < 0$ region, the THz field permits only electrons that travel close to the core to return, thereby reducing the maximum kinetic energy at recombination to $2.69U_p$. These harmonics are emitted at instants approximately $(3.7 + k)T_0$, with $k = 0 - 8$ [see Fig. 2(b1)]. These emission corresponds to the second group of attosecond bursts in Fig. 1(c2), which form the first HHG plateau in Figs. 1[(a),(b2)]. Meanwhile, in the $x > 0$ region, all liberated electrons are pulled back to the core, even those displaced beyond $2r_q$, with traveling times of

up to six optical cycles. The differences in traveling time result in distinct maximum kinetic energies at recombination at instants around $(3.2 + k)T_0$ [25, 26], as illustrated in Fig. 2(b1). This gives rise to the stepwise attosecond bursts of the first group in Fig. 1(c2), accounting for the emergence of the multi-plateau structure in the HHG spectra (Figs. 1[(a),(b2)]). Specifically, under this weak THz field, the long-traveling trajectories can reach a maximum kinetic energy of about $8U_p$, producing high-energy harmonics extending into the EUV and soft X-ray regions.

By increasing the THz strength, e.g., to $\alpha = 10\%$ [Fig. 2(c)] and $\alpha = 40\%$ [Fig. 2(d)], the overall behavior remains similar to the case of $\alpha = 5\%$, except that the furthest displacement of the returning electrons becomes closer to the parent ion. This results in shorter excursion times and, consequently, fewer plateaus in the HHG spectra. At $\alpha = 10\%$, the longest traveling time reduces to three optical cycles, with the maximum kinetic energy reaching $\sim 7.6U_p$. For $\alpha = 40\%$, the strong THz field rapidly drives the electrons back to the ion in the $x > 0$ region, while strongly suppressing their return from the $x < 0$ side. The maximum kinetic energy reaches approximately $9.1U_p$, consistent with previous reports [16, 17, 25, 26, 28, 31].

The most intriguing aspect yet to be clarified is how the THz field governs the maximum kinetic energy gained by the electron dynamics. To address this, Fig. 3(a) shows the variation of the maximum kinetic energy as a function of THz strength, while Fig. 3(b) displays the associated maximum displacement. The corresponding electron excursion time is color encoded.

The dashed black curve in Fig. 3(a) reveals a characteristic “fish-fin” structure, repeatedly reaching about $8U_p$ before attaining the highest value of $9.1U_p$ at $\alpha = 39\%$. This pattern originates from electron trajectories with progressively longer excursion times as the THz field decreases. Each successive “fin ray”, labeled from 1 to 8 in Figs. 3[(a), (b)], corresponds to approximately one additional optical cycle in the excursion time, and is accompanied by the electron being driven progressively farther from the ionic core. Despite the longer excursion times and larger displacements, the maximum kinetic energy quickly saturates at about $8U_p$. Simulations with longer laser pulses confirm that this saturation value is maintained even under much weaker THz fields, albeit at the cost of a significantly larger electron excursion. Table I lists the specific α values corresponding to the local maxima of the kinetic energy and their associated excursion times. These classical behaviors fully explain the fish-fin-shaped overall cutoff and the multi-plateau structure observed in the comprehensive HHG spectra obtained from TDSE simulations, as shown in Fig. 1. The classical “fish-fin” prediction (white solid curve) is in excellent agreement with the numerical results.

Analytical analysis

We now explain the saturated kinetic energy analytically. Following Eq. (3) for the electron motion in the

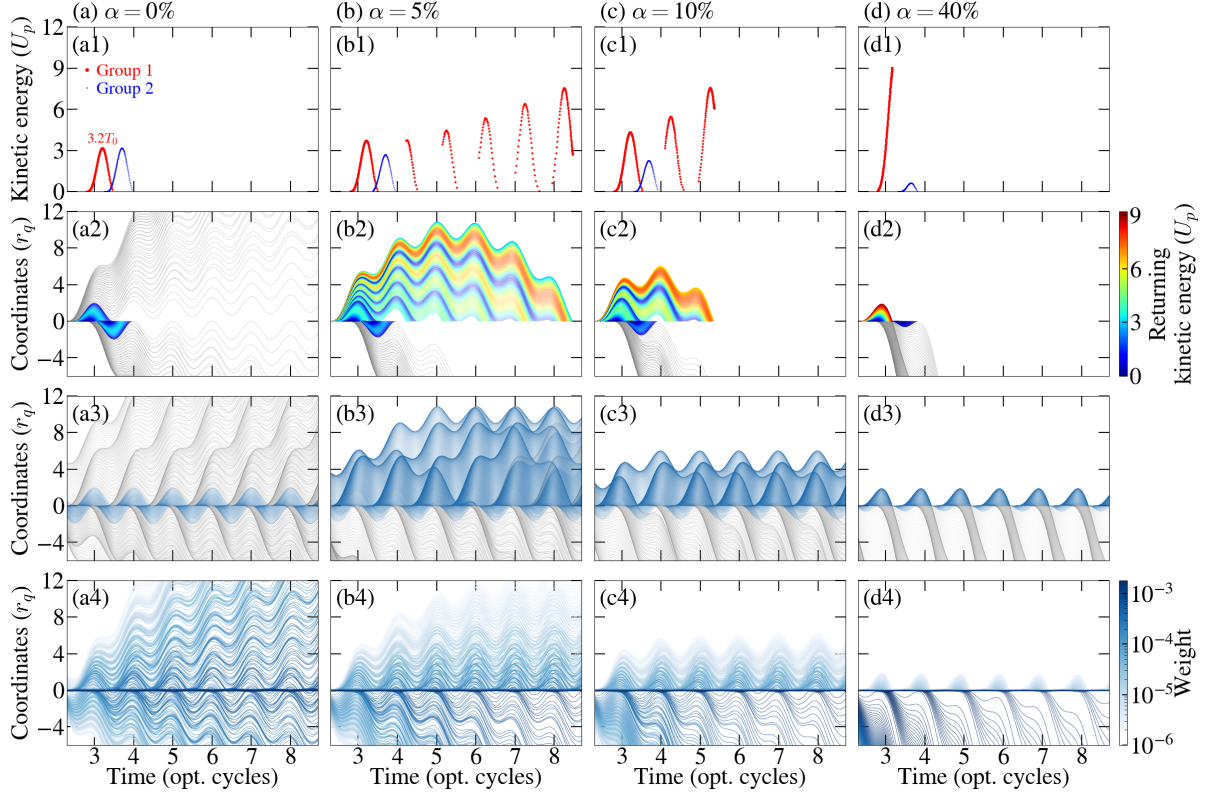


FIG. 2. Classical simulation of returning-electron kinetic-energy at recombination (first row) and electron displacement (second and third rows) for different THz fields with $\alpha = 0, 5\%, 10\%$, and 40% . The corresponding Bohmian trajectories are shown in the last row where the color tone denotes the trajectory weight. For clarity, only electrons liberated within one optical cycle are presented in the first and second rows, while complete trajectories are shown in the third and last rows. In the first row, the blue and red curves represent the electron dynamics responsible for the first and second groups of attosecond bursts in Figs. 1[(c1)-(c4)]. In the second and third rows, gray curves denote all photoelectron trajectories, while colored curves highlight the returning ones whose colors encode their kinetic energy at recombination. The driving IR and THz fields' parameters are the same as in Fig. 1, except for the continuous IR envelope. Long-traveling trajectories lead to distinct burst cutoffs, thereby forming multi-plateau structures and EUV harmonics under moderate THz fields.

TABLE I. Maximum kinetic energy K_{\max} forming each “fin ray” at THz strength α , together with the associated excursion time t_{travel} and maximum displacement A_m obtained from classical simulation. Each “fin ray” is numbered by category. The driving IR and THz fields' parameters are the same as in Fig. 1, except for the continuous IR envelope.

Category	1	2	3	4	5	6	7	8	9	10	11	12	13	14	15	16	17	18	19	20
α (%)	38.6	16.5	10.8	8.0	6.4	5.3	4.6	4.0	3.5	3.2	2.9	2.7	2.4	2.3	2.1	2.0	1.9	1.8	1.7	1.6
K_{\max} (U_p)	9.1	8.2	8.1	8.1	8.0	8.0	8.0	8.0	8.0	8.0	8.0	8.0	8.0	8.0	8.0	8.0	8.0	8.0	8.0	
t_{travel} (T_0)	0.86	1.95	2.96	3.98	4.98	5.98	6.98	7.98	8.99	9.98	10.99	11.99	12.99	13.99	14.99	15.99	16.98	17.99	18.99	20.00
A_m (r_q)	2.0	4.0	5.5	7.2	8.7	10.3	11.9	13.5	15.1	16.6	18.2	19.8	21.4	23.0	24.5	26.1	27.6	29.2	30.8	32.4

combined field $E(t) = E_0 \cos(\omega_0 t) + E_T$, the return condition reads

$$\frac{E_0}{\omega_0^2}(\cos \omega_0 t_r - \cos \omega_0 t_i) + \frac{E_0}{\omega_0} t_e \sin \omega_0 t_i - \frac{E_T}{2} t_e^2 = 0, \quad (5)$$

where $t_e = t_r - t_i$ is the excursion time. For THz-induced long-traveling trajectories where $t_e \gg 2\pi/\omega_0$, this condition simplifies to

$$\frac{E_T}{2} t_e^2 - \frac{E_0}{\omega} t_e \sin \omega_0 t_i \approx 0. \quad (6)$$

The THz field (first term) continuously pushes the electron away from the core, while the oscillating laser field

(second term) pulls it back toward the core. The THz field therefore enables a long excursion time

$$t_e \approx \frac{T_0}{\pi \alpha} \sin \omega_0 t_i \leq \frac{T_0}{\pi \alpha}. \quad (7)$$

The upper limit $t_e^{\max} = \frac{T_0}{\pi \alpha}$ is in good agreement with the maximum excursion time obtained numerically and listed in Tab. I. Owing to the symmetry of the long-traveling returning trajectories, the maximum displacement is reached at half of the excursion time, i.e., at $t_e/2$. The maximum electron displacement can be ap-

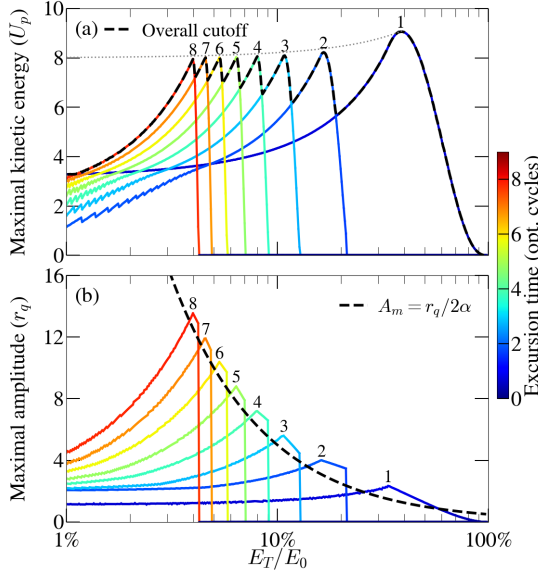


FIG. 3. Maximum kinetic energy (a) and maximum displacement (b) of the returning electron with different excursion time as a function of the THz field strength. The color encodes the electron’s excursion time. In Panel (a), the black dashed curve marks the overall cutoff while the black dotted curve shows the trend of the maximum kinetic energy versus the THz field. The overall cutoff exhibits the “fish-fin” structure of the comprehensive HHG. In Panel (b), the dashed black curve marks the upper limit of returning-electron displacement. As the THz strength decreases, the electron travels farther from the core, and the maximum kinetic energy decreases to a saturated value of about $8.0U_p$.

proximated as

$$A \approx \frac{r_q}{2\alpha} \sin^2 \omega t_i \leq \frac{r_q}{2\alpha}, \quad (8)$$

where $r_q = \frac{E_0}{\omega_0^2}$ is the quiver amplitude of the short trajectory in the absence of the THz field. The upper limit $A_m = \frac{r_q}{2\alpha}$ is shown in Fig. 3(b), in good agreement with the numerical results. Hence, a smaller THz-field α leads to a longer excursion time, enabling the electron to reach a larger displacement while still returning to recombine with the parent ion.

Within this long-traveling approximation, the electron velocity is predominantly gained from the THz field. Consequently, the velocity at the recombination instant is

$$|v(t_r)| \approx E_T t_e \leq \frac{2E_0}{\omega_0}. \quad (9)$$

Thus, the maximum kinetic energy at recombination satisfies $K \leq 8U_p$, yielding a saturated value of $8U_p$, in agreement with the numerical simulations.

In summary, these classical electron dynamics fully account for the THz induced plateau expansion, revealing a field driven mechanism that is fundamentally independent of the target. This independence explains the

remarkable robustness of the “fish-fin” structure across diverse atomic species and highlights its universality as a signature of THz assisted cutoff extension.

2. Bohmian analysis: classical consistency and beyond-classical ionization–recombination insights

We next verify these THz-induced long-traveling trajectories using a quantum-based approach via Bohmian-trajectory analysis. In Figs. 2[(a4)–(d4)], we show a swarm of Bohmian trajectories guided by the quantum wavefunctions describing the electron motion in the combined electric field. These trajectories include all electrons ionized throughout the entire IR pulse. For comparison, the corresponding entire classical trajectories are shown in Figs. 2[(a3)–(d3)].

The figures show that for each value of α , the behaviors of the Bohmian trajectories closely follows that of their classical counterparts. In both descriptions, a subset of trajectories near the origin can return and recombine with the parent ion to generate HHG, while the remaining trajectories are driven away from the core. In the THz-free case [Fig. 2(a4)], the Bohmian trajectories are symmetric about $x = 0$; however, the presence of a THz field breaks this symmetry, as evident in Figs. 2[(b4)–(d4)], producing distinct dynamics in the $x > 0$ and $x < 0$ regions. Electrons in the $x > 0$ region exhibit a higher likelihood of revisiting the parent ion than those in the opposite region. The Bohmian trajectories further reveal that the maximum displacement of recombining trajectories decreases as the THz strength. At $\alpha = 40\%$, long-traveling trajectories no longer exist.

A small difference between the Bohmian and classical trajectories appears at moderate THz strengths. As shown in Figs. 2[(b4)–(c4)], a minor subset of Bohmian trajectories is pushed slightly farther from the core than the classical ones. This deviation originates from quantum effects that are absent in the classical three-step model [49–53]. In the Bohmian picture the motion of the electron is influenced not only by the external field but also by the quantum potential, which reflects the curvature of the wavefunction and produces a small additional spreading of the trajectories. Furthermore, interference between different branches of the tunneling wavefunction can slightly redirect a few trajectories. However, these trajectories have very small probability weight, therefore they do not affect the attosecond-burst cutoff or the resulting HHG cutoff and multiplateau structure.

Furthermore, Bohmian-trajectory swarms not only track electron motion but also provide qualitative access to ionization and recombination probabilities through trajectory counts and weights [49–53], a capability absent in classical simulations. This explains the reduced harmonic yields in the THz-assisted extended plateaus compared with the THz-free case, as shown in Figs. 1[(a), (b1)–(b4)]. Figures 2[(a4)–(d4)] reveal that this reduction arises from two THz-induced effects: a lower liberation probability and a decreased recom-

bination probability, especially in the $x < 0$ region. For weak THz fields, Figs. 2[(b4),(c4)], electrons driven into $x > 0$ acquire distinct excursion times, producing a stepwise decay of higher-plateau intensities. Their long excursions also broaden the returning wave packet, further reducing the recombination probability and suppressing higher-order harmonics. For strong THz fields Figs. 2[(d3),(d4)], dispersion is mitigated by shorter excursions; however, ionization becomes strongly suppressed by ground-state depletion in $x < 0$, leading to a pronounced drop in high-energy harmonic yield.

IV. CONCLUSIONS

In summary, we have investigated plateau extension in THz-assisted HHG using TDSE simulations supported by classical and Bohmian trajectory analyses. We identified a distinct “fish-fin” structure in the comprehensive spectra, whose evolution from $I_p + 9.1U_p$ to the saturated $I_p + 8U_p$ cutoff. This structure reflects the persistence of long-traveling electron trajectories that are sustained by weak to moderately strong THz fields across several optical cycles before recombination. From these dynamics, we established a simple and physically transparent rule linking the attainable cutoff to the maximum excursion time supported at a given THz amplitude. We further showed that this behavior applies broadly to atomic systems provided the IR field remains below the saturation threshold, ensuring that the target does not ionize so rapidly that long trajectories are suppressed.

These findings demonstrate that cutoff control with laboratory level THz fields is feasible and that the “fish-fin” structure serves as a sensitive signature of the underlying electron motion. Importantly, our analysis identifies a clear relation between the THz amplitude, the electron excursion time, and the resulting cutoff position, providing a direct physical rule that can be applied for predictive control of THz assisted HHG. This rule offers practical guidance for enhancing coherent EUV and soft X-ray emission using the weak and moderate THz fields that current laboratories can readily generate.

ACKNOWLEDGMENTS

This research is funded by the Vietnam National Foundation for Science and Technology Development (NAFOSTED) under Grant No. 103.01-2023.138 and carried out by the high-performance cluster at Ho Chi Minh City University of Education, Vietnam. The practice of experimental realization of THz fields was supported by the Russian Science Foundation (RSF), Project No. 25-22-00084.

N.-L. P. and D.-A. T. conceptualized the work, developed the methodology, and carried out the main analytical derivations. D.-A. T., C.-T. L., and N.-L. P. im-

plemented the numerical simulations. D.-A. T., D. D. H.-T., S. H., and N.-H. P. validated the data. F. V. P. provided discussions on experimental feasibility. D.-A. T., N.-L. P., and V.-H. L. contributed to the interpretation of the physical mechanisms. N.-L. P. and V.-H. L. supervised the project. D.-A. T. and N.-L. P. wrote the original draft and finalized the manuscript. All authors discussed the results and contributed to reviewing and editing the manuscript.

APPENDIX A: POTENTIAL MODELS

As discussed in the main text, the THz field drives the liberated electron much farther than in the IR only case, which requires a much larger numerical box and increases computational cost. However, since the IR laser and THz fields are co-linearly polarized, electron motion is primarily along the field direction, making reduced-dimensional models well suited for HHG simulations without substantial loss of accuracy [38, 41, 47]. Recent developments have further improved these models, enabling them to closely reproduce full dimensional harmonic features [41]. In this work, we adopt these advances and employ refined model potentials $V_c(\mathbf{r})$ for diverse atomic targets.

We utilize the density-based one-dimensional (1D) soft-Coulomb potential model [41], which can be written in the form

$$V_c(x) = -\frac{Z/2}{\sqrt{x^2 + 1/4Z^2}}. \quad (10)$$

where $Z = \sqrt{2I_p}$ is the Coulomb charge and I_p is the potential ionization. This model yields ionization energies of 0.50, 0.90, 0.79, and 0.58 a.u. for hydrogen, helium, neon, and argon atoms, respectively, which are in good agreement with experimental values [62]. Moreover, we also produce HHG from the three-dimensional Coulomb potential of a hydrogen atom interacting with a specific combination IR pulse and THz field. The obtained HHG is similar to those calculated using the 1D potential Eq. (10) [38].

APPENDIX B: TDSE METHOD

The time-dependent wavefunction of Eq. (1) is obtained by applying the time evolution operator \hat{U} to the wavefunction at the previous time step

$$\psi_n(t + \Delta t) = \hat{U}(t + \Delta t, t)\psi_n(t), \quad (11)$$

where Δt is the time step. The time propagation is carried out using the split-operator scheme [42–45], where the time evolution operator \hat{U} is factorized into exponential kinetic and potential components as

$$\hat{U}(t + \Delta t, t) \simeq e^{-iV(t)\Delta t/2} e^{-i\hat{T}\Delta t} e^{-iV(t)\Delta t/2}, \quad (12)$$

where $V = V_c + V_{\text{ext}}$ is total potential energy with $V_{\text{ext}} = \mathbf{r} \cdot \mathbf{E}(t)$, and \hat{T} is the kinetic energy operator.

The initial wave-function is required to start the time propagation Eq. (11). This field-free ground state wavefunction $\psi_n(t=0)$ is numerically obtained by using the imaginary-time method [46]. The corresponding conditions to meet the numerical convergence are the imaginary step of 0.02 a.u., and the difference in energy between consecutive iterations does not exceed 10^{-14} a.u..

To perform the simulation, the space is discretized within a simulation box with size of $2 \times (L_x + W_x + 30 \text{ a.u.})$ along the x axis. Here, L_x is the maximal displacement of the liberated electron in the synthesized electric field that can still return to the parent ion, W_x is the width of the $\cos^{1/8}$ -type absorber used to suppress unphysical reflections from the boundaries, and the additional space of 30 a.u. is for keeping the absorber far enough from the target, even in cases where L_x becomes small for specific THz field strengths. We set $W_x = 150 \text{ a.u.} + N_p r_q$, where N_p is number of optical cycle of the IR pulse. A uniform spatial grid of 0.2 a.u. is employed. All parameters are verified to ensure numerical convergence in HHG simulation.

For the calculation of Bohmian trajectories, a large simulation box with a fixed $L_x = 12 r_q$, much larger than that used in the HHG calculations, is employed to ensure that all Bohmian trajectories are captured with-

out artificial absorption. Moreover, a finer spatial grid of 0.02 a.u. is used to improve the resolution of the Bohmian trajectory sampling.

Once the spatiotemporal wavefunction is obtained, the laser-induced acceleration dipole is computed using Ehrenfest's theorem

$$a(t) = -\langle \psi(\mathbf{r}, t) | \nabla V_c(\mathbf{r}) | \psi(\mathbf{r}, t) \rangle - E(t). \quad (13)$$

The HHG spectrum is then obtained by applying the Fourier transform to the acceleration dipole as

$$S(\Omega) = \left| \int_0^\tau a(t) e^{-i\Omega t} dt \right|^2. \quad (14)$$

To resolve the temporal structure of HHG emission, we evaluate the time frequency profile using the Gabor transform [47] as

$$S(\Omega, t) = \left| \frac{1}{\sqrt{2\pi}\sigma} \int_0^\tau a(t') e^{-\frac{(t'-t)^2}{2\sigma^2}} e^{-i\Omega t'} dt' \right|^2. \quad (15)$$

The width σ is set to $0.05T_0$, where $T_0 = 2\pi/\omega_0$ is the optical cycle of the driving laser. This choice provides an appropriate balance between temporal and spectral resolution.

[1] M. Chergui, M. Beye, S. Mukamel, C. Svetina, and C. Masciovecchio, Nat. Rev. Phys. **5**, 578 (2023).

[2] L. Young, K. Ueda, M. Gühr, P. H. Bucksbaum, M. Simon, S. Mukamel, N. Rohringer, K. C. Prince, C. Masciovecchio, M. Meyer, A. Rudenko, D. Rolles, C. Bostedt, M. Fuchs, D. A. Reis, R. Santra, H. Kapteyn, M. Murnane, H. Ibrahim, F. Légaré, M. Vrakking, M. Isinger, D. Kroon, M. Gisselbrecht, A. L'Huillier, H. J. Wörner, and S. R. Leone, J. Phys. B: At. Mol. Opt. Phys. **51**, 032003 (2018).

[3] T. Popmintchev, M.-C. Chen, A. Bahabad, M. Gerrity, P. Sidorenko, O. Cohen, I. P. Christov, M. M. Murnane, and H. C. Kapteyn, Proc. Natl. Acad. Sci. **106**, 10516 (2009).

[4] R. Weissenbilder, S. Carlström, L. Rego, C. Guo, C. Heyl, P. Smorenburg, E. Constant, C. Arnold, and A. L'Huillier, Nat. Rev. Phys. **4**, 713 (2022).

[5] F. Lépine, M. Y. Ivanov, and M. J. Vrakking, Nature Photon. **8**, 195 (2014).

[6] M. Nisoli, P. Decleva, F. Calegari, A. Palacios, and F. Martín, Chem. Rev. **117**, 10760 (2017).

[7] R. Borrego-Varillas, M. Lucchini, and M. Nisoli, Rep. Prog. Phys. **85**, 066401 (2022).

[8] J. Itatani, J. Levesque, D. Zeidler, H. Niikura, H. Pépin, J.-C. Kieffer, P. B. Corkum, and D. M. Villeneuve, Nature **432**, 867 (2004).

[9] G. Vampa and T. Brabec, J. Phys. B: At. Mol. Opt. Phys. **50**, 083001 (2017).

[10] T. T. Luu, Z. Yin, A. Jain, T. Gaumnitz, Y. Pertot, J. Ma, and H. J. Wörner, Nat. Commun. **9**, 3723 (2018).

[11] P. B. Corkum, Phys. Rev. Lett. **71**, 1994 (1993).

[12] M. Lewenstein, P. Balcou, M. Y. Ivanov, A. L'Huillier, and P. B. Corkum, Phys. Rev. A **49**, 2117 (1994).

[13] A. Bandrauk, S. Chelkowski, H. Yu, and E. Constant, Phys. Rev. A **56**, R2537 (1997).

[14] J. J. Carrera and S.-I. Chu, Phys. Rev. A **75**, 033807 (2007).

[15] S.-F. Zhao, X.-X. Zhou, P.-C. Li, and Z. Chen, Phys. Rev. A **78**, 063404 (2008).

[16] W. Hong, P. Lu, W. Cao, P. Lan, and X. Wang, J. Phys. B: At. Mol. Opt. Phys. **40**, 2321 (2007).

[17] W. Hong, P. Lu, P. Lan, Q. Zhang, and X. Wang, Opt. Express **17**, 5139 (2009).

[18] K.-J. Yuan and A. D. Bandrauk, Phys. Rev. A **83**, 063422 (2011).

[19] X.-L. Ge, H. Du, J. Guo, and X.-S. Liu, Opt. Express **23**, 8837 (2015).

[20] T. Severt, J. Troß, G. Kolliopoulos, I. Ben-Itzhak, and C. A. Trallero-Herrero, Optica **8**, 1113 (2021).

[21] S. Petrakis, M. Bakarezos, M. Tatarakis, E. Benis, and N. Papadogiannis, Sci. Rep. **11**, 23882 (2021).

[22] J. Troß, S. Pathak, A. Summers, D. Rompotis, B. Erk, C. Passow, B. Manschwetus, R. Boll, P. Grychtol, S. Bari, V. Kumarappan, A.-T. Le, C. Jin, C. Trallero, and D. Rolles, J. Opt. **24**, 025502 (2022).

[23] A.-K. Raab, M. Schmoll, E. R. Simpson, M. Redon, Y. Fang, C. Guo, A.-L. Viotti, C. L. Arnold, A. L'Huillier, and J. Mauritsson, Rev. Sci. Instrum. **95**, 073002 (2024).

[24] J. Wu, G.-T. Zhang, C.-L. Xia, and X.-S. Liu, Phys.

Rev. A **82**, 013411 (2010).

[25] V. D. Taranukhin and N. Y. Shubin, J. Opt. Soc. Am. B **17**, 1509 (2000).

[26] S. Odžak and D. B. Milošević, Phys. Rev. A **72**, 033407 (2005).

[27] A. Koushki and S. Sarikhani, Chem. Phys. **541**, 111020 (2021).

[28] B. Rumiantsev, E. Migal, A. Pushkin, and F. Potemkin, Phys. Rev. A **111**, 023117 (2025).

[29] X.-L. Ge, Laser Phys. Lett. **17**, 055301 (2020).

[30] M. Mohebbi, Appl. Phys. B **122**, 39 (2016).

[31] B. Wang, X. Li, and P. Fu, Journal of Physics B: Atomic, Molecular and Optical Physics **31**, 1961 (1998).

[32] J. A. Fülöp, S. Tzortzakis, and T. Kampfrath, Adv. Opt. Mater. **8**, 1900681 (2020).

[33] W. J. Choi, M. R. Armstrong, J. H. Yoo, and T. Lee, J. Mater. Chem. C **12**, 9002 (2024).

[34] S. Li, Y. Tang, L. Ortmann, B. K. Talbert, C. I. Blaga, Y. H. Lai, Z. Wang, Y. Cheng, F. Yang, A. S. Landsman, P. Agostini, and L. F. DiMauro, Nat. Commun. **14**, 2603 (2023).

[35] P. A. Shulyndin, B. Rumiantsev, E. A. Migal, A. V. Pushkin, and F. V. Potemkin, JETP Lett. **121**, 846 (2025).

[36] B.-Y. Li, J. Zhang, Y. Zhang, T.-M. Yan, and Y. H. Jiang, Phys. Rev. A **102**, 063102 (2020).

[37] X. Liu, J. Zhang, Y.-K. Fang, G. Yuan, Z. Li, and L.-Y. Peng, Phys. Rev. A **111**, 063103 (2025).

[38] D.-A. Trieu, N.-L. Phan, Q.-H. Truong, H. T. Nguyen, C.-T. Le, D. Vu, and V.-H. Le, Phys. Rev. A **108**, 023109 (2023).

[39] D.-A. Trieu, V.-H. Le, and N.-L. Phan, Phys. Rev. A **110**, L041101 (2024).

[40] D.-A. Trieu, T.-T. D. Nguyen, T.-D. D. Nguyen, T. Tran, V.-H. Le, and N.-L. Phan, Phys. Rev. A **110**, L021101 (2024).

[41] S. Majorosi, M. G. Benedict, and A. Czirják, Phys. Rev. A **98**, 023401 (2018).

[42] S. Z. Burstein and A. A. Mirin, J. Comput. Phys. **5**, 547 (1970).

[43] M. Feit, J. Fleck, and A. Steiger, J. Comput. Phys. **47**, 412 (1982).

[44] K. Mishima and K. Yamashita, J. Chem. Phys. **109**, 1801 (1998).

[45] V. Strelkov, M. Khokhlova, A. Gonoskov, I. Gonoskov, and M. Ryabikin, Phys. Rev. A **86**, 013404 (2012).

[46] R. Kosloff and H. Tal-Ezer, Chem. Phys. Lett. **127**, 223 (1986).

[47] C. Chirilă, I. Dreissigacker, E. V. van der Zwan, and M. Lein, Phys. Rev. A **81**, 033412 (2010).

[48] G. G. Paulus, W. Becker, W. Nicklich, and H. Walther, J. Phys. B: At. Mol. Opt. Phys. **27**, L703 (1994).

[49] D. Bohm, Phys. Rev. **85**, 166 (1952).

[50] J. Wu, B. B. Augstein, and C. Figueira de Morisson Faria, Phys. Rev. A **88**, 023415 (2013).

[51] H. Z. Jooya, D. A. Telnov, and S.-I. Chu, Phys. Rev. A **93**, 063405 (2016).

[52] C.-T. Le, C. Ngo, N.-L. Phan, D. Vu, and V.-H. Le, Phys. Rev. A **107**, 043103 (2023).

[53] C.-T. Le, N.-L. Phan, and V.-H. Le, Phys. Rev. A **110**, 063115 (2024).

[54] N. Takemoto and A. Becker, J. Chem. Phys. **134**, 074309 (2011).

[55] L. V. Keldysh, Zh. Eksperim. i Teor. Fiz. **47** (1964).

[56] T. Brabec and F. Krausz, Rev. Mod. Phys. **72**, 545 (2000).

[57] N.-L. Phan, T.-T. Nguyen, H. Mineo, and V.-H. Hoang, J. Opt. Soc. Am. B **37**, 311 (2020).

[58] G. L. Carr, M. C. Martin, W. R. McKinney, K. Jordan, G. R. Neil, and G. P. Williams, Nature **420**, 153 (2002).

[59] H. Xu, L. Yan, Y. Du, W. Huang, Q. Tian, R. Li, Y. Liang, S. Gu, J. Shi, and C. Tang, Nat. Photonics **15**, 426 (2021).

[60] C. Vicario, A. V. Ovchinnikov, S. I. Ashitkov, M. B. Agranat, V. E. Fortov, and C. P. Hauri, Opt. Lett. **39**, 6632 (2014).

[61] A. Pushkin, E. Migal, D. Suleimanova, E. Mareev, and F. Potemkin, Photonics **9** (2022).

[62] N. I. of Standards and Technology, Security Requirements for Cryptographic Modules, Tech. Rep. Federal Information Processing Standards Publications (FIPS) 140-2, Change Notice 2 December 03, 2002 (U.S. Department of Commerce, Washington, D.C., 2001).